HHS Public Access

Author manuscript

Science. Author manuscript; available in PMC 2025 January 12.

Published in final edited form as:

Science. 2024 January 12; 383(6679): 190–200. doi:10.1126/science.adg1955.

Hyperglycosylation of prosaposin in tumor dendritic cells drives immune escape

Pankaj Sharma[1,†], **Xiaolong Zhang**[1,†], **Kevin Ly**[1,†], **Ji Hyung Kim**[1], **Qi Wan**[1], **Jessica Kim**[1], **Mumeng Lou**[1], **Lisa Kain**[2], **Luc Teyton**[2], **Florian Winau**[1,*]

[1]Program in Cellular and Molecular Medicine, Boston Children's Hospital, Department of Pediatrics, Harvard Medical School, Boston, MA 02115, USA.

[2]Department of Immunology and Microbiology, Scripps Research Institute, La Jolla, CA 92037, USA.

Abstract

Tumors develop strategies to evade immunity by suppressing antigen presentation. In this work, we show that prosaposin (pSAP) drives CD8 T cell–mediated tumor immunity and that its hyperglycosylation in tumor dendritic cells (DCs) leads to cancer immune escape. We found that lysosomal pSAP and its single-saposin cognates mediated disintegration of tumor cell–derived apoptotic bodies to facilitate presentation of membrane-associated antigen and T cell activation. In the tumor microenvironment, transforming growth factor–β (TGF-β) induced hyperglycosylation of pSAP and its subsequent secretion, which ultimately caused depletion of lysosomal saposins. pSAP hyperglycosylation was also observed in tumor-associated DCs from melanoma patients, and reconstitution with pSAP rescued activation of tumor-infiltrating T cells. Targeting DCs with recombinant pSAP triggered tumor protection and enhanced immune checkpoint therapy. Our studies demonstrate a critical function of pSAP in tumor immunity and may support its role in immunotherapy.

Antigen-specific T cell responses are central to protection against cancer. Cytotoxic CD8 T lymphocytes recognize tumor antigens presented by major histocompatibility complex I (MHC-I) molecules and subsequently deploy their effector functions, such as target-cell

*Corresponding author. florian.winau@childrens.harvard.edu.
†These authors contributed equally to this work.

Author contributions: P.S. and F.W. designed the study and performed data analysis. P.S., X.Z., K.L., J.H.K., Q.W., J.K., M.L., and L.K. performed experiments. L.T. produced recombinant pSAP and saposins. P.S. and F.W. wrote the manuscript.

Competing interests: F.W. and P.S. are listed as inventors on a patent application filed by Boston Children's Hospital (provisional application no. 63/350,734), which covers the use of pSAP in cancer therapy. The authors declare no conflict of financial interests.

SUPPLEMENTARY MATERIALS
science.org/doi/10.1126/science.adg1955
Materials and Methods
Figs. S1 to S10
Tables S1 and S2
References (41–46)
MDAR Reproducibility Checklist

killing and production of inflammatory cytokines (1). However, tumor cells often fail to directly activate T cells because of down-regulation of their MHC-I pathway (2, 3). Therefore, other antigen-presenting cells, such as dendritic cells (DCs), are critical to engulf tumor antigens for subsequent processing and display to MHC-I–restricted CD8 T cells in a process called cross-presentation (4). On a cellular level, this mechanism can be broadly divided into a cytosolic and vacuolar pathway (5, 6). According to cytosolic processing, endosomal antigens are retrotranslocated into the cytosol for degradation by proteasomes and subsequent reimport into the endosome for MHC-I loading. By contrast, in the vacuolar pathway, the endosome is more autonomous and relies on its proteases for antigen processing (7–9). Among the different DC subsets, classical DC1s are especially efficient in cross-presentation and fulfill this function in tumor-draining lymph nodes for T cell priming as well as in the tumor microenvironment to activate tumor-infiltrating T lymphocytes (10, 11). Abundance and proper function of immune cells, including antigen-presenting cells and lymphocytes, at the tumor site are vital for effective immunity and control of cancer growth (12, 13). Unfortunately, tumors often develop mechanisms to evade immune responses; for example, by producing immunosuppressive cytokines such as transforming growth factor–β (TGF-β) (14, 15). Thus, the goal of cancer therapy is to target and overcome immune evasion to restore protective immunity.

Prosaposin (pSAP) is a precursor protein that is transported from the Golgi apparatus to the lysosome, assisted by its chaperone, sortilin (16, 17). In the lysosome, cathepsins cleave pSAP into the single saposins A to D. Saposins are also called sphingolipid activator proteins because they function as small, nonenzymatic cofactors for lysosomal hydrolases that are required for sphingolipid degradation (18). Moreover, at the low acidic pH of the endolysosomal compartment, saposins are able to interact with anionic phospholipids, such as phosphatidylserine (PS), exposed on intralysosomal vesicles (19). These membrane-perturbing properties facilitate vesicle disintegration and pertain to apoptotic vesicles that characteristically contain PS in their lipid bilayers (20, 21). In this context, tumors, owing to their uncontrolled growth kinetics, produce a substantial amount of dying cells and apoptotic bodies that contain tumor antigens to potentially trigger the immune system. Notably, membrane-associated particulate antigen is more immunogenic than soluble protein, and thus, antigen presentation pathways based on vesicular processing might be central to the induction of protective T cell immunity. In this study, we explored the impact of saposins on presentation of membrane-associated tumor antigen and activation of CD8 T cell responses that protect against cancer growth. This work also describes a mechanism by which the tumor counteracts saposin-mediated processing by triggering pSAP hyperglycosylation and secretion from tumor-associated DCs. Ultimately, we tested the proof-of-principle of pSAP targeting to DCs as a possible mode of cancer immunotherapy.

Results

Saposins promote cross-presentation of membrane-associated tumor antigen

First, we investigated the effect of saposins on the integrity of apoptotic bodies derived from tumor cells. For this purpose, we exposed murine MCA fibrosarcoma cells to γ irradiation [100 Gy (unit of absorbed dose of ionizing radiation); 1 Gy = 100 rads] to trigger apoptotic

cell death (Fig. 1A). Successful induction of apoptosis was controlled by measuring PS exposure with AnnexinV staining. Subsequently, we purified apoptotic vesicles from cell culture supernatants using differential ultracentrifugation (100,000*g* pellets) and visualized them by transmission electron microscopy (Fig. 1B). We then loaded the fluorescent dye calcein into those apoptotic vesicles using a liposome extruder with a 100-nm pore size. After incubation with different recombinant saposins, we measured calcein release and found that saposins disintegrate tumor cell–derived apoptotic vesicles when compared with control bovine serum albumin (BSA) (Fig. 1B). In addition to leakage of the small molecule calcein, we also tested whether saposins facilitate vesicular release of larger proteins and incubated liposomes enclosing fluorescein isothiocyanate (FITC)–labeled ovalbumin (OVA-FITC) with single saposins. In contrast to incubation with BSA, saposins triggered the release of soluble OVA protein, with various saposins exhibiting different membrane-perturbing potency (fig. S1A).

We next explored the impact of saposins on the processing of apoptotic bodies in DCs. To this end, we first assessed the subcellular localization of pSAP in the endosomal or lysosomal compartments using DC2.4 cells (murine DC line) transfected with a pSAP expression vector containing a C-terminal FLAG tag. We found maximum colocalization of pSAP with LAMP-1 protein, indicating its predominant distribution in lysosomes (fig. S1B). Next, we pulsed bone marrow–derived DCs with carboxyfluorescein diacetate succinimidyl ester (CFSE)–labeled apoptotic cells derived from γ-irradiated MCA101 tumor cells and followed their fate along the endolysosomal compartment. Confocal microscopy revealed colocalization of apoptotic bodies with LAMP-1, which indicated trafficking to saposin-containing lysosomes (Fig. 1C). When comparing the kinetic digestion of apoptotic cells in pSAP-deficient or wild-type (WT) DCs, we found that early uptake of apoptotic material was similar, suggesting that phagocytosis is not affected by saposin deficiency. However, at later time points after endocytosis, pSAP-deficient DCs accumulated CFSE-labeled cells, demonstrating the importance of saposins for processing of apoptotic bodies in DCs (Fig. 1D).

To test for saposin-dependent cross-presentation and CD8 T cell activation, we pulsed DCs from pSAP-knockout (KO) or WT mice with apoptotic MCA101 cells expressing a membrane-associated form of the antigen OVA prior to coculture with OVA-specific CD8 T cells. MCA101-OVA cells express the model antigen coupled to the C1C2 domain of lactadherin, which allows for targeting of OVA to PS-expressing vesicles (22). We analyzed productive antigen processing by staining for the processed OVA epitope in complex with MHC-I (H-2K^{b}-SIINFEKL) on the DC surface. Flow cytometry demonstrated that processing of soluble OVA was equally efficient in pSAP-KO and WT DCs (Fig. 1E). However, processing and MHC-I loading of membrane-associated antigen derived from tumor cells was significantly hampered in the absence of pSAP (Fig. 1E). These findings were in accordance with our T cell data, as pSAP-deficient DCs efficiently activated CD8 T cells in response to soluble antigen as well as OVA-coated latex beads (Fig. 1F and fig. S1C). In sharp contrast, when DCs were pulsed with tumor cells containing membrane-associated antigen, CD8 T cell activation by pSAP-KO DCs was greatly reduced, as highlighted by their truncated CFSE dilution profile in flow cytometry (Fig. 1G). Notably, incubation of pSAP-deficient DCs with recombinant pSAP fully reconstituted CD8 T cell

activation (Fig. 1G). Similarly, we pulsed pSAP-KO or WT DCs with irradiated B16F10 melanoma cells prior to coculture with antigen-specific CD8 T cells that recognize the integral membrane protein Pmel-1 (gp100). Impaired T cell activation by pSAP-deficient DCs revealed that saposins are equally important for processing of membrane-associated melanoma antigens (fig. S1D). In addition, pSAP deficiency also compromised MHC-II–restricted presentation of tumor antigens derived from apoptotic bodies, as indicated by diminished stimulation of antigen-specific CD4 T cells (fig. S1E). Taken together, saposins disintegrate apoptotic vesicles and process membrane-associated antigens for presentation to CD4 and CD8 T cells.

pSAP is required for tumor immunity

Next, we investigated how pSAP function affects T cell activation in vivo and protection against cancer. To assess T cell priming, we transferred naïve CFSE-labeled, OVA-specific CD8 T cells into pSAP-deficient or WT recipients prior to subcutaneous administration of apoptotic MCA101-OVA cells (fig. S2A). Four days after tumor cell injection, we isolated DCs from skin-draining lymph nodes and analyzed antigen processing. Expression of H-2K^{b}-SIINFEKL proved to be reduced in DCs from pSAP-KO when compared with that of WT mice (fig. S2B). Moreover, antigen-specific proliferation and interferon (IFN)–γ production by CD8 T cells from lymph nodes were severely hampered in the absence of pSAP (fig. S2C). Thus, pSAP facilitates CD8 T cell priming in response to particulate antigen. Because straight pSAP-KO mice have a reduced life span, we generated chimeric mice by transferring pSAP-KO or WT bone marrow to WT recipients to allow for tumor challenge experiments. In this context, we immunized mice with irradiated tumor cells and challenged them with a higher number of live MCA101-OVA cells one week later (Fig. 2A). Subsequently, we monitored tumor growth in the skin and found a drastic expansion of cancer in pSAP deficiency (Fig. 2B). Flow cytometry analysis of isolated DCs from the tumor site showed a pSAP-dependent decrease in antigen processing and presentation (Fig. 2C). Furthermore, MHC-I tetramer–mediated detection of antigen-specific CD8 T cells showed reduced frequency of tumor-infiltrating T cells as well as cytokine production in pSAP-deficient mice (Fig. 2D). Additionally, we also challenged bone marrow–chimeric mice with live tumor cells without prior vaccination (fig. S3A). As a result, cancer protection, antigen processing in tumor DCs, frequency of tumor-infiltrating, antigen-specific T cells, and cytokine production and cytotoxicity were all greatly reduced when pSAP was lacking (fig. S3, B to E). To exclude that pSAP-dependent tumor immunity was influenced by differential DC migration, we examined migratory DCs in tumor-draining lymph nodes and found no alteration in DC frequencies and expression of the homing marker CCR7 in pSAP deficiency (fig. S3, F and G). Moreover, we analyzed DC-attracting chemokines at the tumor site and observed comparable expression of CCL19 and CCL21 in pSAP-KO and WT mice (fig. S3H). Because pSAP has been associated with macrophage function and inflammation (23), we controlled our mouse model for a possible impact on tumor-associated macrophages. However, pSAP deficiency neither affected the number of macrophages nor their expression of inflammatory genes in the tumor microenvironment (TME) (fig. S3, I and J). Altogether, these findings demonstrate that tumor immunity critically depends on pSAP function.

T lymphocytes from melanoma patients are boosted by pSAP

To study pSAP in the context of human cancer, we used dissociated tumor cell samples from melanoma patients. A detailed description of the patient samples can be found in table S1. Briefly, the majority of specimens were isolated from primary melanoma lesions of the skin, assigned as clinical stage III, including those from white female and male patients older than 50 years before treatment (table S1). To purify antigen-presenting cells, responder T cells, and tumor cells as source of antigen, we used fluorescence-activated cell sorting (FACS) on $CD146^+$ melanoma cells, $CD11b/c^+$ myeloid cells, and $CD8^+$ T cells (fig. S4). We then irradiated $CD146^+$ melanoma cells and pulsed them onto sorted myeloid cells prior to coculture with autologous CD8 T cells (Fig. 2E). In parallel, we also treated DCs and T cells with human recombinant pSAP. Five days after culture, we analyzed effector functions of CD8 T cells and found that recombinant pSAP was able to boost IFN-γ production (Fig. 2F) and cytolytic activity, indicated by surface LAMP-1 staining as a sign of cytotoxic degranulation (Fig. 2G). Furthermore, we measured the frequencies of tumor antigen–specific CD8 T cells by staining with MHC-I tetramers loaded with dominant melanoma antigens, including MART, gp100, tyrosinase, and NY-ESO-1. The abundance of melanoma-specific CD8 T cells was greatly increased when tumor DCs were treated with pSAP (Fig. 2H). Notably, the patient samples were human leukocyte antigen (HLA)–typed by flow cytometry beforehand to select the proper haplotype for MHC-I tetramer analysis (HLA-A02). Overall, the impact of pSAP on tumor DCs is able to rescue T cell activation from melanoma patients.

Hyperglycosylation of pSAP in tumor DCs leads to its secretion

Beyond the use of pSAP deficiency in a mouse model, we aimed at understanding the regulation of pSAP in tumor-associated DCs in a pathophysiological context. To this end, we inoculated WT mice with live MCA101-OVA cells subcutaneously, and after tumor outgrowth, we isolated DCs from the TME, tumor-draining lymph nodes, and spleen (fig. S5A). We FACS-purified the two main classical DC subsets on the basis of their established markers as cDC1 ($XCR1^+$ or $CD103^+$) and cDC2 ($SIRP1a^+$ or $CD11b^+$) prior to performing an array of antigen processing and presentation assays. Accordingly, pulsing with FITC-dextran showed that the phagocytosis rate of tumor DCs was not altered when compared with lymph node and spleen (fig. S5B). Incubation with a self-quenched antigen conjugate (DQ-OVA), which exhibits fluorescence upon proteolytic degradation, demonstrated that mainly cDC2s in the tumor are compromised to process soluble antigen (fig. S5C). These findings were in line with the ultimate epitope expression on surface MHC-I following pulsing with soluble OVA, which revealed hampered antigen presentation by tumor cDC2 (fig. S5D). In sharp contrast, the presentation capacity of cDC1 in the TME was only affected after incubation with irradiated MCA101-OVA cells, which contain antigen in membrane-associated form (fig. S5D). This phenomenon was reflected in functional T cell experiments because DCs isolated from tumors were severely perturbed to induce T cell responses reactive to membrane-associated antigen (fig. S5E).

Because we found that saposins are critical for presentation of particulate antigen, we then hypothesized that pSAP function might be modulated in tumor DCs as a basis for poor T cell induction in the TME. Indeed, analysis by immunoblot revealed the expression of a

75-kDa high molecular weight form of pSAP in tumor DCs when compared with pSAP-65, which was predominant in DCs from spleen (Fig. 3A). Moreover, the small, single saposins were severely depleted in DCs from the TME (Fig. 3A). When we cultured the respective DC subsets ex vivo, we observed secretion of pSAP into the cell culture supernatant mainly by tumor DCs (Fig. 3, A and B). To demonstrate that the occurrence of pSAP-75 was due to glycosylation, we tested endoglycosidase H (Endo H) sensitivity of pSAP. Endo H cleaves N-linked glycans between the two proximal N-acetylglucosamine residues only in high-mannose carbohydrate chains, but not in complex glycans. After treatment of protein lysates with Endo H, pSAP-65 from splenic DCs was cleaved to lower molecular weight forms, whereas pSAP-75 from tumor DCs proved to be Endo H–resistant, suggesting that it contains complex glycans (Fig. 3C). To corroborate this finding, we performed deeper molecular analysis using mass spectrometry of sugar structures based on purified pSAP bands derived from splenic (pSAP-65) or tumor DCs (pSAP-75). Tandem mass spectrometry showed that the glycan of pSAP-65 mainly consisted of mannose residues, whereas pSAP-75 exhibited complex glycans involving additions of N-acetylglucosamine, galactose, and sialic acid (Fig. 3D). Because glycan structures are synthesized by a diverse set of glycosyltransferases, we compared the expression of glycosyltransferases between tumor and splenic DCs using a quantitative reverse transcription polymerase chain reaction (qRT-PCR) array (Fig. 3E). In tumor DCs, we found up-regulation of several enzymes that facilitate the attachment of complex glycan residues, such as N-acetylglucosaminyltransferases, galactosyltransferases, and sialyltransferases (Fig. 3F).

Because hyperglycosylation of pSAP leads to its secretion and therefore, the reduced generation of single saposins, we next investigated the interaction of pSAP with its chaperone sortilin, which is normally required for efficient lysosomal delivery of pSAP. For this purpose, we subjected tumor and splenic DCs to a proximity ligation assay (PLA), in which antibodies against pSAP and sortilin are coupled to oligonucleotide probes that allow for subsequent ligation and amplification in case the two target proteins are in close vicinity (10 to 80 nm). Confocal microscopy revealed these PLA events as discrete spots and showed that the spatial relationship between pSAP and sortilin was perturbed in DCs from the TME (Fig. 3G). To assess the direct physical interaction between pSAP and sortilin through biochemistry, we performed immunoprecipitation of pSAP and subsequently resolved sortilin using immunoblot. As a result, the abundance of sortilin recovered from the pSAP precipitate was clearly reduced in tumor DCs, indicating that the interaction of pSAP with its chaperone sortilin is hampered in the TME (Fig. 3H). To translate these findings to the human system, we explored pSAP-sortilin interaction in DCs isolated from the tumor site of melanoma patients compared with that of monocyte-derived DCs. The resulting PLA signals demonstrated that the spatial interaction of pSAP with sortilin was reduced in melanoma DCs (Fig. 3I). Furthermore, we examined the abundance of the different molecular weight forms of pSAP and found that tumor DCs from melanoma patients exclusively expressed hyperglycosylated pSAP-75 (Fig. 3J).

Taken together, our results demonstrate that pSAP is hyperglycosylated in tumor DCs, fails to interact with its chaperone sortilin, and follows instead a secretory route (Fig. 3K). This mechanism of pSAP hyperglycosylation leads to a depletion of intracellular saposins

available for antigen processing, which might explain the compromised antigen presentation capacity in the tumor microenvironment.

TGF-β induces pSAP hyperglycosylation in tumor DCs and drives immune evasion

We mechanistically addressed the question how hyperglycosylation of pSAP is regulated. To this end, we screened a panel of recombinant cytokines upon incubation of a murine DC line (DC2.4) and found that TGF-β can induce pSAP secretion (fig. S6A). Treatment of DCs with TGF-β triggered dose-dependent induction of pSAP-75 and subsequent secretion into the culture supernatant, as detected by immunoblot and enzyme-linked immunosorbent assay (ELISA), without affecting the expression of the pSAP chaperone, sortilin (Fig. 4, A to D). Moreover, we measured the gene expression of a panel of enzymes involved in the glycosylation pathway in DC2.4 cells treated with TGF-β (fig. S6B). We observed that the up-regulated genes in TGF-β–treated DCs correlated well with the enzyme signature detected in tumor DCs (Fig. 4E), suggesting that TGF-β is responsible for triggering the respective glycosylation program. To test whether TGF-β signaling is indeed required for pSAP hyperglycosylation in vivo, we used mice that lacked TGF-β receptor II specifically in DCs (CD11c-Cre × $Tgfbr2^{flox/flox}$) for challenge with live MCA101-OVA tumor cells (Fig. 4F). As anticipated, the lack of TGF-β downstream signaling in DCs caused better tumor protection, increased antigen presentation in tumor DCs, and stronger IFN-γ production by tumor-infiltrating CD8 T cells (Fig. 4, G to I). More notably, when we isolated DCs, macrophages, and other $CD45^+$ leukocytes from the tumor site for analysis by immunoblot, we found that pSAP-75 was specifically absent in DCs that lacked TGF-β signaling, whereas the expression of sortilin in tumor DCs was not dependent on TGF-β (Fig. 4, J and K). Additionally, tumor DCs lacking TGF-β receptor exhibited an abundance of single saposins, which was in great contrast to the saposin depletion and exclusive expression of hyperglycosylated pSAP (pSAP-75) in WT DCs as well as tumor-associated macrophages and other $CD45^+$ leukocytes (Fig. 4J). Furthermore, the enzyme signature involved in glycosylation proved to be reduced when TGF-β signaling was deficient in tumor DCs (Fig. 4L).

Next, we investigated how TGF-β mechanistically mediates the glycan complexity of pSAP and its effects on sortilin interaction and pSAP secretion. Our mass spectrometry data revealed that the complex glycan of pSAP-75 is generated through the addition of N-acetylglucosamine, galactose, and sialic acid to the ternary mannose core (Fig. 3D and fig. S7A). On the basis of this observation, we hypothesized that TGF-β controls pSAP hyperglycosylation by modulating the expression of specific enzymes involved in glycan synthesis. Analyzing our gene expression array, we selected TGF-β–induced N-acetylglucosaminyltransferases (Mgat4a and Mgat5) and galactosyltransferase (B4galt1) based on their relevance in the corresponding pSAP glycan pathway identified by mass spectrometry (fig. S7A). In addition to the TGF-β–regulated enzymes, the pSAP glycan pathway is complemented by constitutive glycosyltransferases, such as Mgat1/2, which synthesize precursor molecules for Mgat4a and Mgat5, as well as the sialyltransferases St6Gal1 and St6Gal2 that add terminal sialic acid to the carbohydrate chain generated by B4galt1 (fig. S7A). Subsequently, we performed small interfering RNA (siRNA)–mediated knockdown of those enzyme candidates in TGF-β–treated DC2.4 cells (fig. S7, B and

C) prior to testing the impact on pSAP interaction with sortilin using PLA, pSAP secretion based on ELISA, and T cell activation using antigen presentation assays. As a negative control, we chose the TGF-β–regulated enzyme Mgat3 that produces a bisecting N-acetylglucosamine on the trimannosyl core, which represents a carbohydrate structure absent from our mass spectrometry data on pSAP-75 and therefore is not expected to play a role in the pSAP glycan pathway (fig. S7B).

Notably, the silencing of all pSAP-75–associated glycosyltransferases restored the interaction of pSAP with sortilin, as indicated by drastically amplified PLA signal (fig. S7D). By contrast, knockdown of negative control Mgat3 had no effect on pSAP-sortilin engagement (fig. S7D). In a complementary manner, down-regulation of the respective enzyme candidates prevented the release of pSAP into the supernatant of DCs and facilitated proper CD8 T cell activation, whereas Mgat3 modulation failed to affect pSAP secretion and T cell induction (fig. S7, E and F). Notably, gene silencing of St6Gal enzymes was sufficient to reconstitute the pSAP-sortilin PLA signal, implicating terminal sialic acid residues as critical blockers of this interaction. To confirm these findings, we used an established inhibitor of sialyltransferase (3F-NeuAc) upon incubation of TGF-β–treated DC2.4 cells (fig. S7G), which completely abrogated the addition of sialic acid to the pSAP glycan, as indicated by ELISA-based binding of a lectin specific for sialic acid (fig. S7H). Consistent with the siRNA results, inhibition of pSAP sialylation reinstated its interaction with sortilin and prevented eventual secretion, thereby promoting activation of CD8 T cells (fig. S7, I to K). These data indicate that TGF-β–regulated Mgat and B4galt1 enzymes are crucial for the sequential synthesis of the complex pSAP glycan and that terminal sialylation by St6Gal impedes the pSAP and sortilin interaction.

Furthermore, we examined the molecular mechanism of TGF-β downstream signaling and its regulation of signature enzymes involved in pSAP hyperglycosylation. For this purpose, we performed chromatin immunoprecipitation of the signal transducers Smad2/3 using genomic DNA derived from TGF-β–treated DC2.4 cells (fig. S7L). When compared with isotype control immunoglobulin G (IgG) and the housekeeping gene β-actin, subsequent amplification by PCR revealed significant enrichment of promoter regions containing Smad-responsive elements in the genes coding for Mgat4a, Mgat5, and B4galt1 (fig. S7L).

Taken together, these findings demonstrate (i) the constitutive and TGF-β–regulated enzyme pathway required for the generation of hyperglycosylated pSAP, (ii) the critical function of terminal sialic acid to hamper interaction with sortilin, and (iii) the presence of TGF-β–responsive gene promoter sequences in signature enzymes involved in pSAP glycan synthesis. Overall, TGF-β is essential for hyperglycosylation of pSAP in tumor DCs, a mechanism associated with immune escape.

Immunotherapeutic targeting of tumor DCs with recombinant pSAP

Based on the importance of pSAP for antigen presentation in the tumor microenvironment, we then aimed at targeting recombinant pSAP to tumor DCs. For this purpose, we coupled pSAP to anti-DEC205, an antibody well established to target the endocytic receptor DEC205 on DCs, using chemical conjugation as previously described (24, 25). Briefly, we incubated recombinant pSAP with tris (2-carboxyethyl) phosphine hydrochloride to

expose its sulfhydryl groups, and in parallel, the anti-DEC205 antibody or isotype control IgG were activated for chemical conjugation by sulfosuccinimidyl 4-[N-maleimidomethyl] cyclohexane-1-carboxylate. Following overnight incubation, the pSAP-antibody conjugates were concentrated, and successful coupling was analyzed by immunoblot (fig. S8A). In addition, we controlled that the amount of pSAP coupled to anti-DEC205 or isotype control was comparable (fig. S8B). Moreover, we verified that pSAP conjugation still preserved the fine specificity of the DEC205 antibody by showing that the pSAP–anti-DEC205 conjugate stained a similar percentage of DCs when compared to separate anti-DEC205 detection by flow cytometry (fig. S8C). Furthermore, we incubated pSAP-KO DCs with the pSAP-antibody conjugates and tested OVA epitope expression and CD8 T cell activation after the pulsing of DCs with apoptotic MCA101-OVA cells (fig. S8D). Accordingly, we observed reconstitution of antigen presentation (H-2K^b-SIINFEKL) and CD8 T cell priming (CD69) specifically by pSAP coupled to anti-DEC205 in a dose-dependent manner (fig. S8, E and F). To assess the impact of glycosylation on pSAP's biological activity, we purified pSAP-65 and pSAP-75 from DC2.4 cells. Treatment of pSAP-65 with peptide N-glycosidase (PNGase) F generated nonglycosylated pSAP-55 (fig. S8G). Subsequently, we coupled the differentially glycosylated pSAP forms with anti-DEC205 and incubated pSAP-KO DCs with the conjugates prior to performing functional T cell assays. In contrast to pSAP-65, hyperglycosylated and nonglycosylated pSAP mediated significantly lower CD8 T cell activation (fig. S8H), which highlights that optimal glycosylation of pSAP is required for deploying its functions in the context of endosomal delivery by pSAP-based therapeutics.

After validation of the targeting tool in vitro and ex vivo, we inoculated pSAP-KO bone marrow–chimeric mice with MCA101-OVA tumor cells and injected 100 μg of pSAP coupled with anti-DEC205 or isotype IgG on days 9 and 13 after tumor challenge (Fig. 5A). On day 14, we isolated and sorted intratumoral DCs, focusing on the two major classical DC subsets, cDC1 and cDC2. Staining for intracellular pSAP in the respective DC subsets revealed effective delivery of pSAP targeted through DEC205 when compared with the isotype control (Fig. 5B). Additionally, immunoblot analysis revealed that pSAP-deficient tumor DCs took up recombinant pSAP-65 and generated massive amounts of single saposins upon lysosomal cleavage (Fig. 5C). This demonstrated successful reconstitution of pSAP-deficient DCs in the TME, especially in the cDC1 subtype that is central to cross-priming of CD8 T cells. We then followed a similar experimental schedule using pSAP targeting of tumor-inoculated WT animals (Fig. 5D). Treatment with pSAP coupled to anti-DEC205 greatly reduced tumor burden in WT mice (Fig. 5E). Correspondingly, antigen presentation of OVA peptide by tumor DCs as well as frequency of IFN-γ-producing, antigen-specific T cells at the tumor site and in draining lymph nodes (dLNs) were significantly amplified upon pSAP treatment (Fig. 5, F to H).

Moreover, we investigated whether pSAP therapy is able to amplify antitumor memory. To this end, we first subcutaneously administered 1×10^6 MCA101-OVA tumor cells into the left flank of WT mice prior to treatment with 100 μg of pSAP coupled to anti-DEC205 or isotype IgG (fig. S8I). When tumors reached a volume of ~600 mm^3, mice were anesthetized and tumors were surgically removed, followed by tumor cell rechallenge into the contralateral side (fig. S8I). Monitoring tumor volume after rechallenge revealed that

DC-targeted pSAP treatment significantly reduced tumor growth (fig. S8J). This increased protection was reflected in a drastic expansion of antigen-specific CD8 T cells at the tumor site (fig. S8K). These data suggest that pSAP-based immunotherapy drives immunological memory toward tumor protection.

Because pSAP delivery to tumor DCs promoted an immunologically active TME, we next asked whether pSAP could also rescue immune suppression in immunologically cold tumors. For this purpose, we used the B16F10 melanoma model that displays limited T cell infiltration and low susceptibility to treatment with immune checkpoint inhibitors such as anti–PD-1 despite strong expression of PD-L1 (26, 27). When compared with mice treated with anti–PD-L1 alone, the tumor growth kinetics revealed that pSAP combination therapy was able to overcome the resistance of B16F10 melanoma to immune checkpoint blockade in order to enable protection (Fig. 5I). Furthermore, pSAP combination therapy led to significantly increased frequencies of total CD4 and CD8 T cells among various subsets of tumor-infiltrating immune cells (fig. S9, A and B). Notably, treatment with recombinant pSAP and immune checkpoint blockade activated CD8 T cells, amplified the frequencies of T lymphocytes specific for the melanoma antigen Pmel-1 (gp100), and facilitated robust cytokine production (fig. S9, C and D).

On the basis of our results that genetic ablation of TGF-β signaling in DCs fully abrogates pSAP hyperglycosylation and secretion, we investigated whether restored antigen presentation could increase the susceptibility of $Tgfbr2^{\Delta DC}$ mice to anti–PD-L1 treatment in the B16F10 melanoma model. Our tumor challenge data show that the intrinsic loss of TGF-β signaling in DCs indeed enhances the responsiveness to immune checkpoint blockade (fig. S9E).

Taken together, these results highlight the crucial impact of pSAP on antigen presentation by tumor DCs to trigger powerful intratumoral T cell responses and point to a viable future strategy for immunotherapy of cancer.

Discussion

In this work, we demonstrated the critical function of saposins in the processing of corpuscular, membrane-associated antigens required for efficient CD8 T cell activation. Notably, saposins were not essential for cross-presentation of soluble antigen, which mechanistically involves a rather early endosomal or phagosomal compartment (6). In cancer immunity, the provision of particulate antigen derived from dying tumor cells represents a physiologic and potent route of antigen delivery. In this context, it has been shown that only DCs that contain tumor-derived vesicles are able to induce T cell responses (28). Thus, our findings highlight the importance of the lysosome in the cross-priming of T cells and underscore the impact of saposins on the immunogenic pathway of vesicular processing.

In tumor biology, previous reports suggested a trophic function of pSAP stimulating the proliferation of cancer cells (29, 30). However, pSAP and a pSAP-derived synthetic cyclic peptide were able to prevent tumor metastasis in a mouse model (31, 32). Our work

established a genuine immunological function of pSAP in tumor DCs. Thus, pSAP-driven antigen processing and presentation at the tumor site amplified abundance and functionality of tumor-infiltrating T lymphocytes, ultimately leading to cancer control.

TGF-β is a pleiotropic cytokine with a diverse set of immunosuppressive functions and is also produced by most cell types. Therefore, tumors themselves, as well as the infiltrating cells of the TME, can serve as the source and target of TGF-β. For example, tumor-derived TGF-β is capable of restricting T cell infiltration or functionally blocking differentiation of protective T lymphocyte populations (15, 33). Our results revealed that TGF-β acts on tumor DCs to trigger hyperglycosylation of pSAP and its subsequent secretion, depleting the lysosomal pool of saposins required for proper antigen processing and presentation (fig. S10). The secretion of pSAP has been shown to be caused by pSAP oligomerization in a cell line (34). However, in primary DCs in the tumor microenvironment, we did not observe large oligomers and instead found perturbed interaction between sortilin and hyperglycosylated pSAP. An additional lysosomal player called progranulin might be involved in this mechanism, as it has been shown to bridge the interaction between pSAP and sortilin (35). Overall, tumors are prone to immune escape, and our work describes a further cancerous strategy to manipulate an antigen processing molecule through glycosylation.

Because hyperglycosylation of pSAP occurs along the secretory pathway, an approach to overcome tumor-induced saposin deficiency entails the feeding of recombinant pSAP into the endocytic route of DCs (fig. S10). In this context, our targeting experiments using pSAP coupled to anti-DEC205 demonstrated that reconstitution with fully functional pSAP can restore antigen presentation in tumor DCs, leading to amplified T cell responses and eventual tumor protection. DCs are not only crucial for T cell priming in draining lymph nodes; a growing body of evidence indicates that tumor-associated DCs have vital functions regarding recruitment of effector T cells and stimulation of tumor-infiltrating T lymphocytes, which are overall required for effective immunity to cancer (36–39). Current therapeutic options, such as immune checkpoint blockade, aim at reinvigorating exhausted T cells to augment antitumor responses (40). However, these boosted T lymphocytes need to encounter their respective antigens to deploy their functions in a tumor-specific manner. Consistent with that notion, we showed that pSAP combination treatment can override the resistance of immunologically cold tumors to immune checkpoint inhibitors. Taken together, a pSAP-based therapy might help to restore powerful antigen presentation by tumor DCs with the goal of driving protective immune responses at the site of the cancer.

Supplementary Material

Refer to Web version on PubMed Central for supplementary material.

ACKNOWLEDGMENTS

We thank C. Théry for providing us with OVA-expressing MCA101 fibrosarcoma cells. We are grateful to R. Cummings, S. Lehoux, and all members of the National Center for Functional Glycomics (NCFG) at Harvard Medical School for performing glycan mass spectrometry. Illustrations used in the manuscript were created using BioRender.com.

Funding:

This work was supported by National Institutes of Health grant R01 AI136939 to F.W.

Data and material availability:

Gene expression data have been deposited to Gene Expression Omnibus and are available under accession number GSE248278. Mass spectrometry data are available from GlycoPOST (ID: GPST000381). All data are available in the manuscript or the supplementary materials.

REFERENCES AND NOTES

1. Vesely MD, Kershaw MH, Schreiber RD, Smyth MJ, Annu. Rev. Immunol 29, 235–271 (2011). [PubMed: 21219185]
2. Rooney MS, Shukla SA, Wu CJ, Getz G, Hacohen N, Cell 160, 48–61 (2015). [PubMed: 25594174]
3. Sade-Feldman M et al., Nat. Commun 8, 1136 (2017). [PubMed: 29070816]
4. Alloatti A et al., J. Exp. Med 214, 2231–2241 (2017). [PubMed: 28663435]
5. Blum JS, Wearsch PA, Cresswell P, Annu. Rev. Immunol 31, 443–473 (2013). [PubMed: 23298205]
6. Blander JM, Annu. Rev. Immunol 36, 717–753 (2018). [PubMed: 29490164]
7. Shen L, Sigal LJ, Boes M, Rock KL, Immunity 21, 155–165 (2004). [PubMed: 15308097]
8. Saveanu L et al., Science 325, 213–217 (2009). [PubMed: 19498108]
9. Tang-Huau TL et al., Nat. Commun 9, 2570 (2018). [PubMed: 29967419]
10. Hildner K et al., Science 322, 1097–1100 (2008). [PubMed: 19008445]
11. Ferris ST et al., Nature 584, 624–629 (2020). [PubMed: 32788723]
12. Gajewski TF, Schreiber H, Fu YX, Nat. Immunol 14, 1014–1022 (2013). [PubMed: 24048123]
13. Wculek SK et al., Nat. Rev. Immunol 20, 7–24 (2020). [PubMed: 31467405]
14. Flavell RA, Sanjabi S, Wrzesinski SH, Licona-Limón P, Nat. Rev. Immunol 10, 554–567 (2010). [PubMed: 20616810]
15. Mariathasan S et al., Nature 554, 544–548 (2018). [PubMed: 29443960]
16. Lefrancois S, Zeng J, Hassan AJ, Canuel M, Morales CR, EMBO J. 22, 6430–6437 (2003). [PubMed: 14657016]
17. Yuan L, Morales CR, J. Histochem. Cytochem 58, 287–300 (2010). [PubMed: 19934382]
18. Darmoise A, Maschmeyer P, Winau F, Adv. Immunol 105, 25–62 (2010). [PubMed: 20510729]
19. Kolter T, Sandhoff K, Annu. Rev. Cell Dev. Biol 21, 81–103 (2005). [PubMed: 16212488]
20. Ciaffoni F et al., J. Biol. Chem 276, 31583–31589 (2001). [PubMed: 11406625]
21. Winau F et al., Immunity 24, 105–117 (2006). [PubMed: 16413927]
22. Zeelenberg IS et al., Cancer Res. 68, 1228–1235 (2008). [PubMed: 18281500]
23. van Leent MMT et al., Sci. Transl. Med 13, eabe1433 (2021).
24. Jiang W et al., Nature 375, 151–155 (1995). [PubMed: 7753172]
25. Volckmar J et al., J. Vis. Exp (168): (2021).
26. Fidler IJ, Cancer Res. 35, 218–224 (1975). [PubMed: 1109790]
27. Quezada SA et al., J. Exp. Med 205, 2125–2138 (2008). [PubMed: 18725522]
28. Ruhland MK et al., Cancer Cell 37, 786–799.e5 (2020). [PubMed: 32516589]
29. Jiang Y et al., J. Pathol 249, 26–38 (2019). [PubMed: 30953361]
30. Ishihara S, Inman DR, Li WJ, Ponik SM, Keely PJ, Cancer Res. 77, 6179–6189 (2017). [PubMed: 28972074]
31. Kang SY et al., Proc. Natl. Acad. Sci. U.S.A 106, 12115–12120 (2009). [PubMed: 19581582]
32. Wang S et al., Sci. Transl. Med 8, 329ra34 (2016).
33. Liu M et al., Nature 587, 115–120 (2020). [PubMed: 33087928]

34. Yuan L, Morales CR, Exp. Cell Res 317, 2456–2467 (2011). [PubMed: 21835174]
35. Zhou X et al., Nat. Commun 8, 15277 (2017). [PubMed: 28541286]
36. Salmon H et al., Immunity 44, 924–938 (2016). [PubMed: 27096321]
37. Spranger S, Dai D, Horton B, Gajewski TF, Cancer Cell 31, 711–723.e4 (2017). [PubMed: 28486109]
38. Jang JE et al., Cell Rep. 20, 558–571 (2017). [PubMed: 28723561]
39. Barry KC et al., Nat. Med 24, 1178–1191 (2018). [PubMed: 29942093]
40. Sharma P et al., Cancer Discov. 11, 838–857 (2021). [PubMed: 33811120]

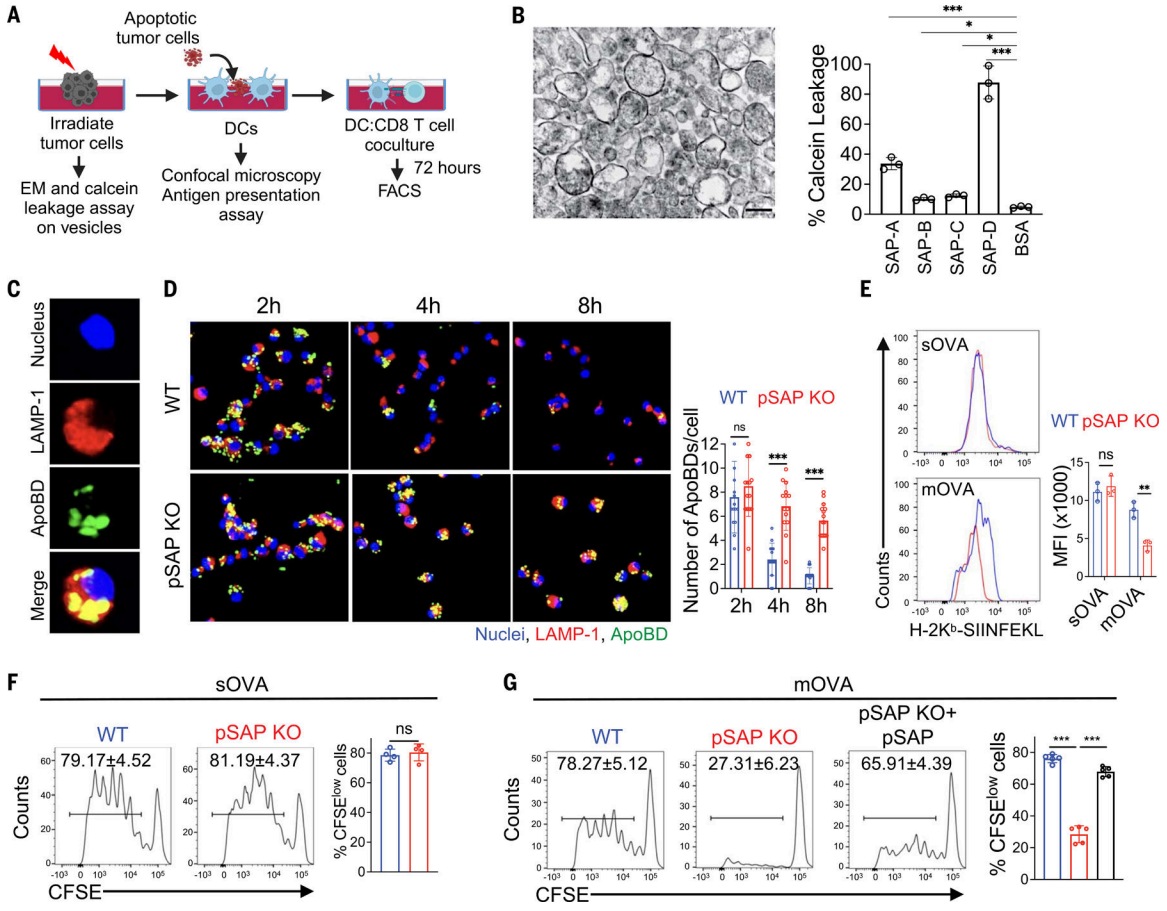

Fig. 1. Saposins promote cross-presentation of membrane-associated tumor antigens.

(**A**) Diagram depicting the experimental read-outs used in Fig. 1. MCA101 fibrosarcoma cells were γ-irradiated (100 Gy) prior to the collection of apoptotic vesicles from supernatant and analysis with electron microscopy (EM) and calcein leakage assay. Apoptotic MCA101 or MCA101-OVA cells were used to pulse bone marrow–derived DCs from WT or pSAP-KO mice prior to the analysis of digestion of apoptotic cells with confocal microscopy and antigen processing and T cell activation with FACS. (**B**) Calcein leakage assay to quantify the effect of saposins on disintegration of apoptotic bodies. Apoptotic vesicles were prepared with differential ultracentrifugation (100,000*g*) from the supernatant of irradiated MCA101 cells and visualized with transmission electron microscopy (left). Scale bar, 200 nm. Apoptotic bodies were further loaded with calcein dye prior to incubation with indicated saposins or BSA (negative control), and calcein release was quantified in the supernatant with fluorimetry. (Right) Depicted is percent leakage compared with 100% lysis induced by Triton X-100. SAP, saposin. (**C**) Representative confocal microscopy image showing colocalization of apoptotic bodies (green) with LAMP-1 (red). WT DCs were pulsed with CFSE-labeled, γ-irradiated apoptotic MCA101 tumor cells for 2 hours. ApoBD, apoptotic body. (**D**) Representative confocal microscopy images showing the kinetics of apoptotic cell disintegration in WT and pSAP-KO DCs. DCs were pulsed with CFSE-labeled, γ-irradiated apoptotic MCA101 tumor cells for 2 hours, and the numbers of apoptotic bodies (ApoBD) were quantified at the indicated time

points with ImageJ software (DAPI, blue; LAMP-1, red; ApoBD, green). (**E**) Representative histogram overlays and bar graph showing flow cytometry staining and mean fluorescence intensity (MFI) of MHC-I-SIINFEKL peptide on the surface of WT or pSAP-KO DCs after incubation with either soluble OVA (sOVA) or irradiated MCA101-OVA tumor cells (mOVA, membrane-associated OVA) for 4 hours. (**F**) Histograms and bar graph showing frequencies of proliferating $CFSE^{low}$ CD8 T cells after a three-day coculture with WT or pSAP-KO DCs pulsed with soluble OVA. (**G**) Histograms and bar graph depicting the frequencies of $CFSE^{low}$ CD8 T cells after a three-day coculture with WT or pSAP-KO DCs pulsed with irradiated MCA101-OVA cells. Additionally, pSAP-KO DCs were reconstituted with 10 μg/ml of recombinant pSAP prior to the T cell assay. Data shown in all graphs represent mean ± SD from three to five independent replicates. *P* values were determined with one-way analysis of variance (ANOVA) [(B) and (G)] or unpaired Student's *t* test [(D), (E) and (F)]. $*P < 0.05$; $**P < 0.01$; $***P < 0.001$; ns, not significant.

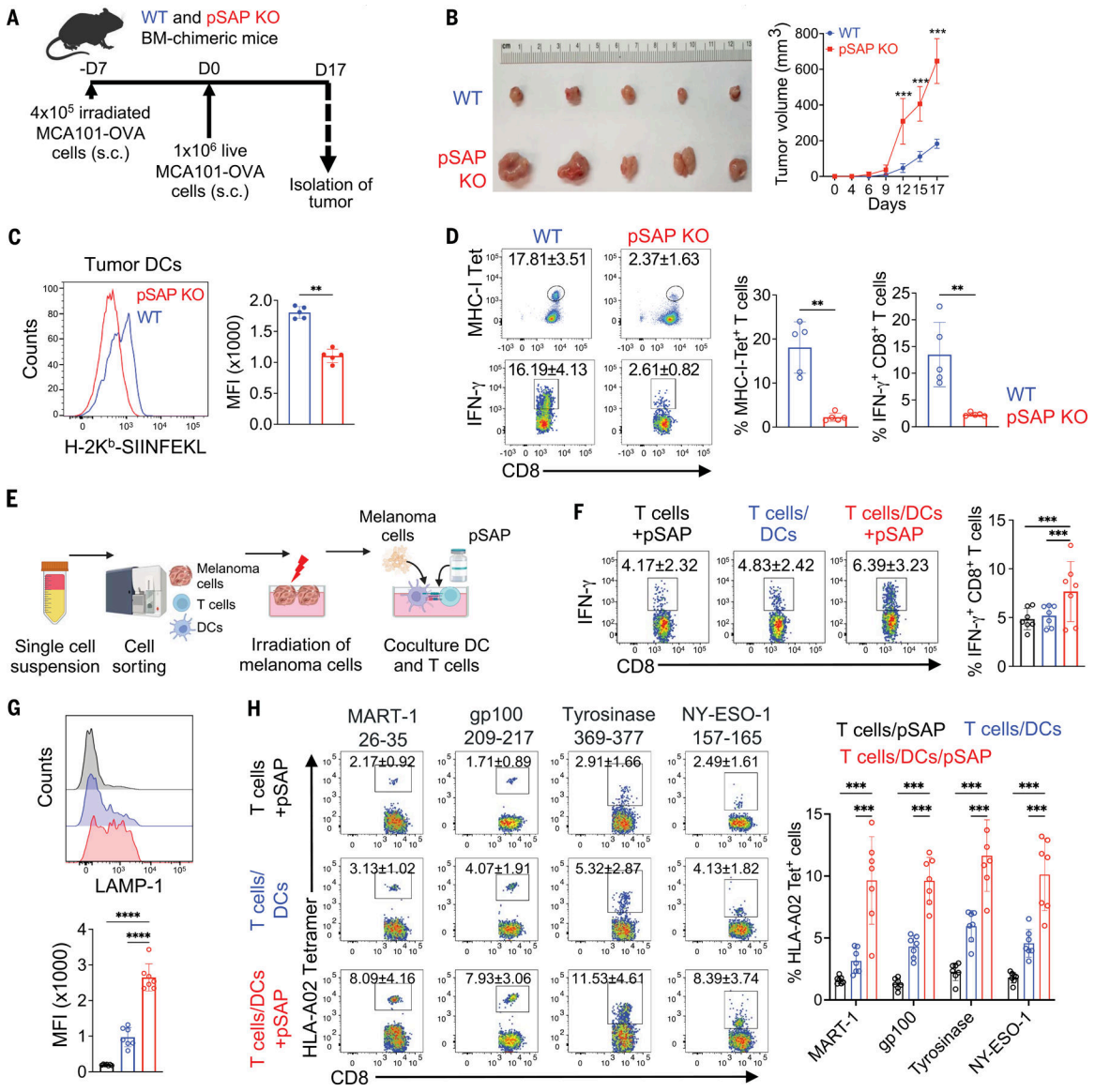

Fig. 2. pSAP is required for tumor immunity and boosts T cells derived from melanoma patient samples.

(**A**) Experimental scheme of tumor challenge studies. WT and pSAP-KO BM chimeric mice were primed with 4×10^5 γ-irradiated MCA101-OVA cells subcutaneously (s.c.) and subsequently inoculated with 1×10^6 live MCA101-OVA cells (s.c.) 7 days post priming (D0). (**B**) Comparison of tumor sizes between WT and pSAP-KO mice on day 17 (left) and the kinetics of the tumors' growth (right). (**C**) Representative histogram overlay and bar graph depicting the staining and MFI of MHC-I-SIINFEKL peptide on the surface of tumor DCs from pSAP-KO or WT animals. (**D**) FACS plots and bar graphs showing frequencies of MHC-I (Kb-SIINFEKL) tetramer- and IFN-γ–positive tumor-infiltrating CD8 T cells in pSAP-KO or WT mice. MHC-I tetramer specifically detects CD8 T cells that are reactive with SIINFEKL peptide. (**E**) Experimental setup for the coculture of myeloid and CD8 T cells isolated from human melanoma. Single-cell suspensions from human melanoma samples were FACS-sorted for $CD146^+$ melanoma cells, $CD8^+$ T cells, and

CD11c/b$^+$ myeloid cells. CD146$^+$ cells were γ-irradiated and incubated with DCs, which were further cocultured with CD8 T cells in the presence or absence of recombinant pSAP. (**F**) FACS plots and bar graph showing the frequencies of IFN-γ–positive CD8 T cells following the indicated culture conditions. (**G**) Representative histogram overlay and bar graph demonstrating surface staining and MFI of LAMP-1 on CD8 T cells according to the indicated culture conditions. Graph colors represent the same as in (F). (**H**) Flow cytometry analysis and summarizing bar graph depicting the frequencies of antigen-specific CD8 T cells reactive with HLA-A*0201 tetramers loaded with epitopes from gp100, MART-1, tyrosinase, and NY-ESO-1 following the indicated culture setups. Amino acid residues are depicted on top, and percentages of gated cells are shown as mean ± SD in the dot plots. Data shown in (B) to (D) are representative of three independent experiments, whereas (F) to (H) depict mean ± SD from seven independent subjects. *P* values were determined by unpaired Student's *t* test [(B) to (D)] or one-way ANOVA [(F) to (H)]. $^{**}P < 0.01$; $^{***}P < 0.001$; $^{****}P < 0.0001$.

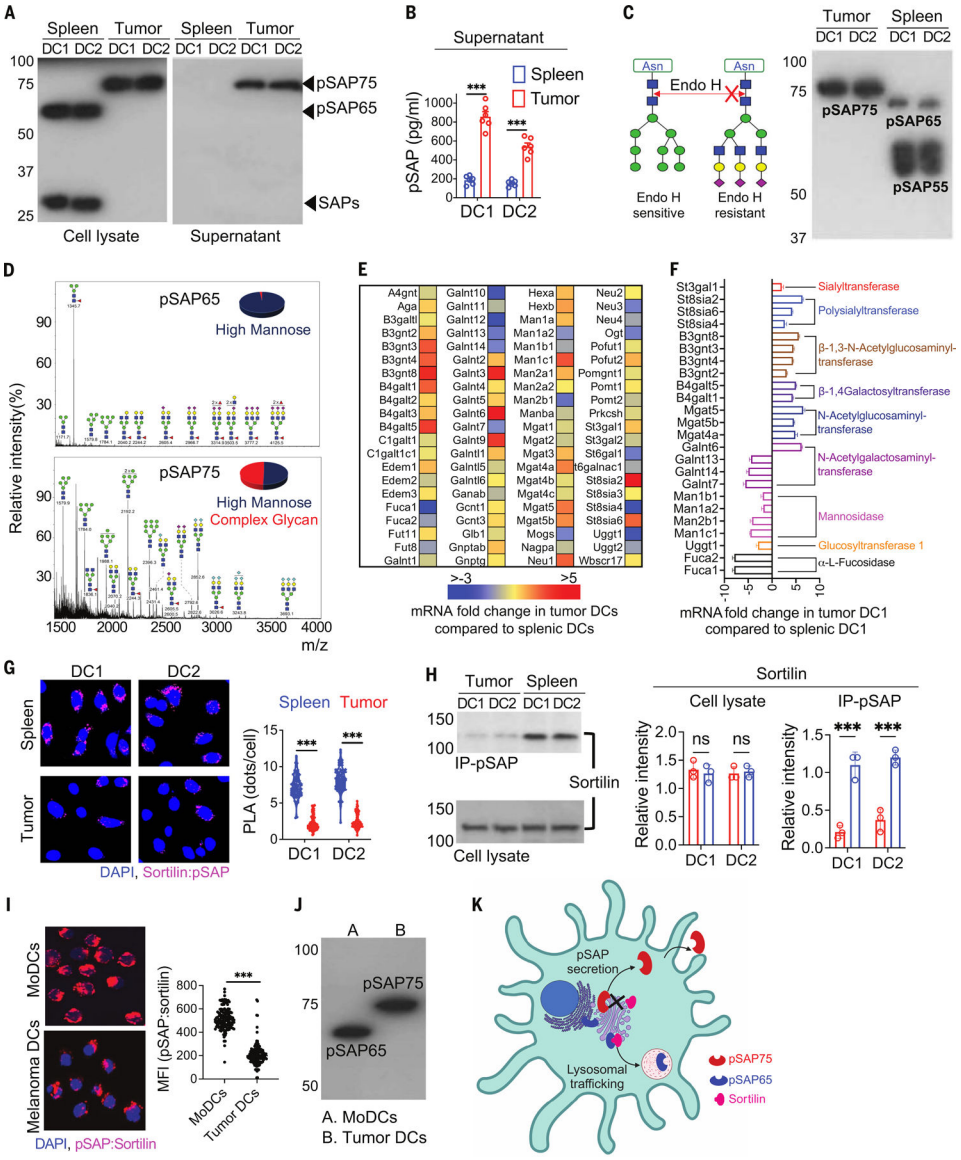

Fig. 3. Hyperglycosylation of pSAP in tumor DCs leads to its secretion.

WT mice were inoculated with 1×10^6 live MCA101 cells, and 18 days post tumor inoculation, cDC1 and cDC2 populations were FACS-sorted from tumor and spleen. (**A**) Immunoblot showing the abundance of pSAP and saposins in DCs as well as pSAP secretion. The left blot shows the expression of pSAP and saposins in FACS-sorted DC subsets from tumor and spleen, whereas the right blot shows secreted pSAP in the culture supernatant. pSAP-75, hyperglycosylated pSAP; pSAP-65, glycosylated pSAP; SAPs, saposins. (**B**) Quantification of pSAP secreted by DCs. FACS-sorted splenic and tumor DC subsets were cultured in cRPMI for 48 hours, and pSAP in culture supernatant was quantified with ELISA. (**C**) Immunoblot of Endo H–treated pSAP. (Left) Mechanism of Endo H that leads to cleavage of high-mannose, but not complex, glycans. (Right) FACS-sorted DCs from tumor and spleen were lysed in radioimmunoprecipitation assay (RIPA) buffer and cell lysates were treated with Endo H for 12 hours at 37°C prior to

analysis with immunoblot. (**D**) Matrix-assisted laser desorption/ionization–time-of-flight (MALDI-TOF) mass spectrometry analysis of permethylated N-linked glycans of pSAP immunoprecipitated from FACS-sorted $CD11c^+$ DCs. Enzymatically released N-glycans from pSAP of splenic (top) and tumor (bottom) DCs were analyzed. Glycan compositions were assigned based on m/z values. *x* axis, mass to charge ratio (m/z). *y* axis, signal intensity of the ions. green circle, mannose; yellow circle, galactose; red triangle, fucose; blue square, N-acetylglucosamine; magenta diamond, sialic acid. (**E**) Heat map of differentially expressed genes in tumor DCs involved in glycosylation, as analyzed by real-time RT^2 profiler PCR array. Splenic DCs were used as the control to calculate fold change in gene expression. (**F**) Bar graph depicting glycosyltransferase and glycosidase gene expression in tumor compared with that of splenic DC1. (**G**) PLA of pSAP and sortilin. Confocal microscopy images of tumor and splenic DC subsets reveal PLA signal between pSAP and sortilin. Blue indicates cell nucleus (DAPI) and magenta represents ligation signal. The violin plot shows quantification of PLA signal, where 200 cells from each sample were analyzed for statistics. (**H**) Coimmunoprecipitation of sortilin and pSAP in tumor and splenic DCs. (Top) Blot of sortilin pulled down by anti-pSAP antibody. (Bottom) Immunoblot of total sortilin in corresponding DC populations. Bar graphs depict the densitometric and statistical analysis of sortilin abundance in the immunoblots. Red, tumor; blue, spleen. IP-pSAP, immunoprecipitation of pSAP. (**I**) PLA of pSAP and sortilin in human melanoma and monocyte-derived DCs (MoDCs). Melanoma DCs were sorted as $CD11c^+$ cells from viable $CD45^+$ cells isolated from human melanoma samples, whereas MoDCs were generated by culturing monocytes with interleukin 4 (IL-4) and granulocyte-macrophage colony-stimulating factor (GM-CSF) for 4 days. Blue indicates cell nucleus (DAPI), and magenta represents ligation signal. The violin plot shows quantification of PLA signal, where 200 cells from each sample were analyzed for statistics. (**J**) Immunoblot of pSAP in human melanoma DCs and MoDCs. (**K**) Illustration visualizing glycosylation mechanisms that control pSAP trafficking in tumor DCs. Hyperglycosylation of pSAP compromises its interaction with sortilin and reroutes it to the secretory pathway. Data shown in all graphs are representative of three independent experiments, and *P* values were determined with unpaired Student's *t* test. $*P < 0.05$; $**P < 0.01$; $***P < 0.001$; $****P < 0.0001$; ns, not significant.

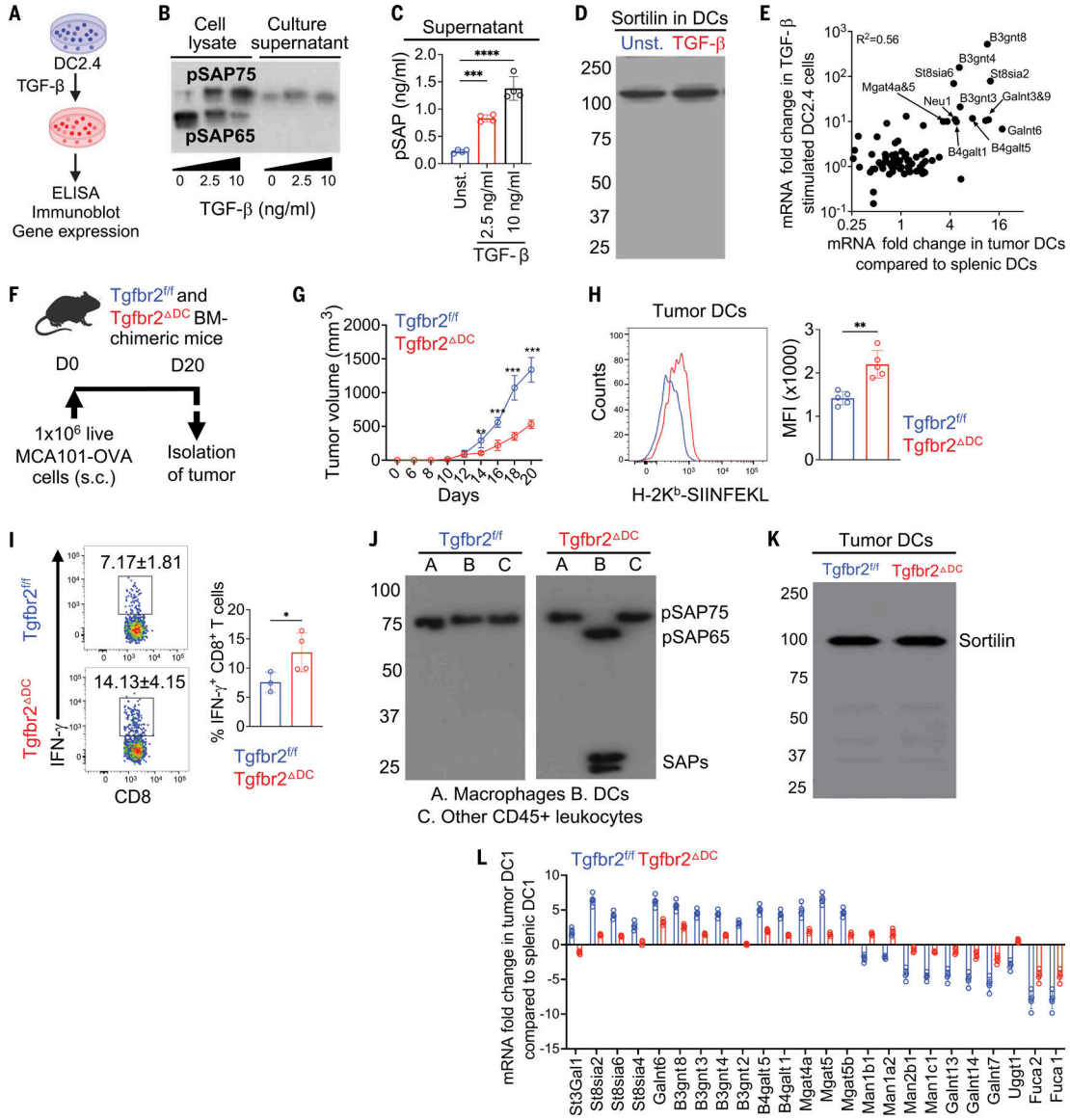

Fig. 4. TGF-β induces pSAP hyperglycosylation in DCs and compromises tumor immunity.

(**A**) Experimental setup of murine DC (DC2.4) cells treated with TGF-β and read-outs shown in (B) to (E). (**B**) Immunoblot showing dose-dependent induction of pSAP hyperglycosylation and secretion by DC2.4 cell line incubated with recombinant TGF-β for 48 hours. (**C**) Quantification of pSAP in the culture supernatant of DC2.4 cells after incubation with recombinant TGF-β for 2 days as measured with ELISA. Unst., unstimulated. (**D**) Immunoblot of sortilin in DC2.4 cells after incubation with recombinant TGF-β for 2 days. (**E**) Scatter plot showing the correlation of gene expression of glycosyltransferases and glycosidases between tumor DCs and TGF-β–stimulated DC2.4 cells. mRNA fold changes were quantified by real-time RT^2 profiler PCR array. $CD11c^+$ tumor DCs were analyzed with splenic DCs as the control, whereas TGF-β-stimulated DC2.4 cells were compared with sham-treated DC2.4 cells. (**F**) Experimental scheme of tumor cell challenge. $Tgfbr2^{f/f}$ and CD11c–Cre × $Tgfbr2^{f/f}$ ($Tgfbr2^{\Delta DC}$) BM chimeric mice

were inoculated with 1×10^6 live MCA101-OVA cells (s.c.). (**G**) Kinetics of tumor growth in Tgfbr2$^{f/f}$ and Tgfbr2$^{\Delta DC}$ mice. (**H**) Histogram overlay and bar graph depicting H-2K^b-SIINFEKL staining and MFI on tumor DCs from Tgfbr2$^{\Delta DC}$ mice or Tgfbr2$^{f/f}$ controls on day 20 after tumor cell injection. (**I**) FACS plots and bar graph showing frequencies of IFN-γ^+ tumor-infiltrating CD8 T cells in Tgfbr2$^{\Delta DC}$ or Tgfbr2$^{f/f}$ animals on day 20 post tumor challenge. (**J**) Immunoblot of pSAP and saposins (SAPs) in tumor DCs, macrophages, and other CD45$^+$ leukocytes from Tgfbr2$^{\Delta DC}$ or Tgfbr2$^{f/f}$ mice on day 20 after tumor cell inoculation. (**K**) Immunoblot of sortilin in tumor DCs from Tgfbr2$^{\Delta DC}$ or Tgfbr2$^{f/f}$ mice on day 20 after tumor cell inoculation. (**L**) Differentially expressed glycosyltransferase and glycosidase genes in tumor DCs isolated from Tgfbr2$^{\Delta DC}$ or Tgfbr2$^{f/f}$ mice on day 20 after tumor challenge. Splenic DCs from Tgfbr2$^{f/f}$ animals were used as control to calculate mRNA fold change. Data shown in all graphs are representative of three independent experiments, and *P* values were determined with one-way ANOVA (C) or unpaired Student's *t* test [(G) to (I)]. **P* < 0.05; ***P* < 0.01; ****P* < 0.001; *****P* < 0.0001.

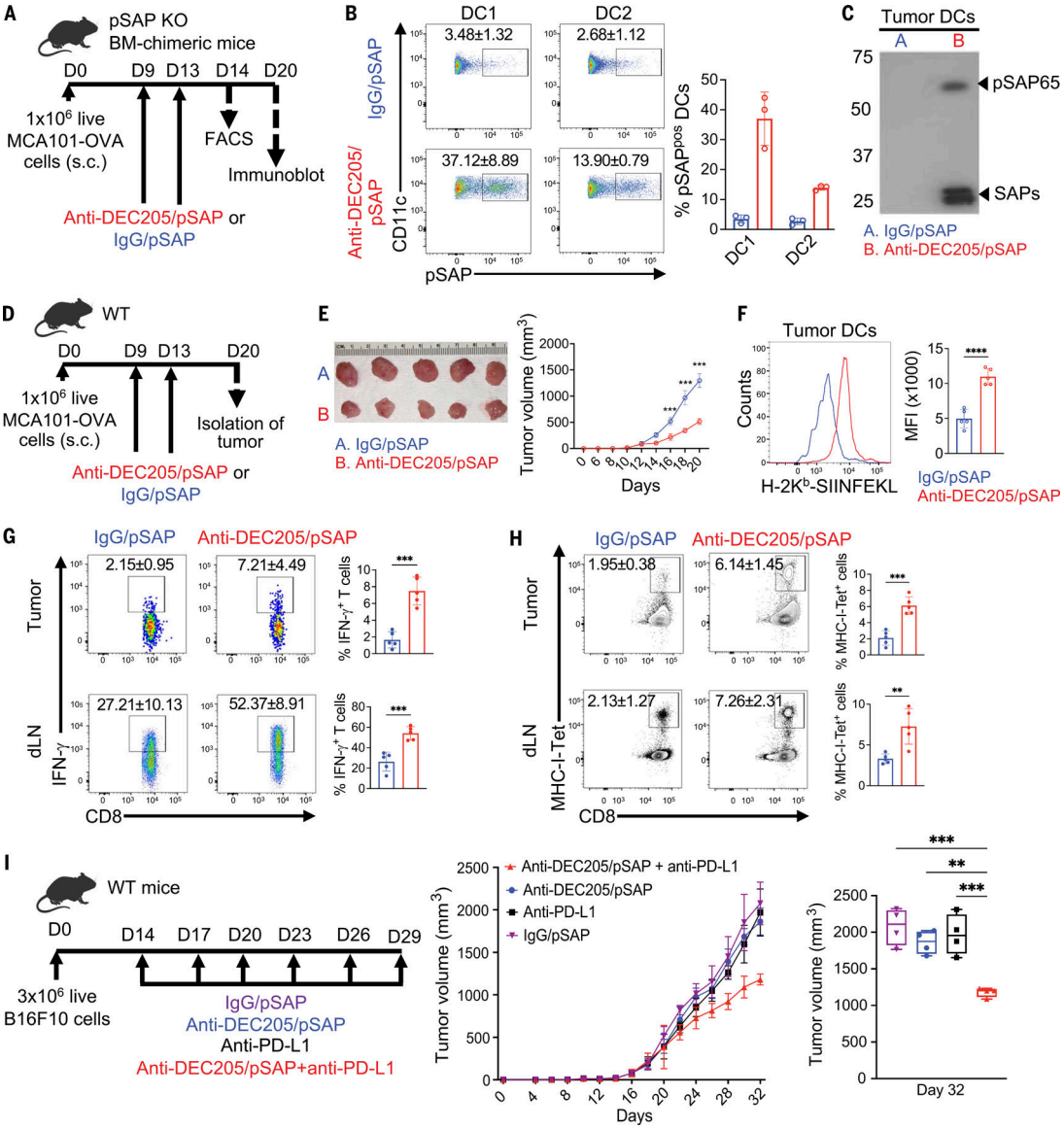

Fig. 5. Reconstitution of tumor DCs with recombinant pSAP drives protection from cancer.

(**A**) Regime of pSAP targeting to tumor DCs. pSAP-KO BM-chimeric mice were inoculated with 1 × 10^6 live MCA101-OVA cells. On days 9 and 13 after tumor cell injection, mice were intravenously treated with pSAP coupled with either anti-DEC205 or isotype control antibodies. (**B**) FACS plots and bar graph showing the amount of pSAP uptake by DCs at the tumor site as analyzed on day 14 after tumor challenge. (**C**) Immunoblot of delivered pSAP and single saposins in pSAP-deficient tumor DCs on day 20 after tumor cell inoculation. (**D**) Experimental setup depicting tumor cell inoculation and pSAP targeting through DEC205 in WT mice. (**E**) Comparison of tumor sizes on day 20 (left) and kinetics of tumor growth (right). (**F**) Histogram overlay and bar graph showing H-2K^b-SIINFEKL peptide surface staining and MFI on tumor DCs on day 20 post tumor challenge. (**G**) FACS plots and bar graphs showing percentages of IFN-γ–positive CD8 T cells in tumors and dLNs in mice treated with pSAP coupled to anti-DEC205 or isotype control. (**H**) Flow cytometry and

bar graphs showing MHC-I (K^b-SIINFEKL) tetramer (MHC-I-Tet)–positive CD8 T cells in tumors and dLNs. (**I**) Experimental setup depicting B16F10 melanoma cell inoculation, pSAP targeting through DEC205, and tumor growth kinetics. WT mice were inoculated with 3×10^6 live melanoma cells and were treated with pSAP coupled with anti-DEC205 or isotype control antibodies, either alone or in combination with anti–PD-L1 antibodies. Statistical analysis of tumor volume across all treatment groups is shown on day 32 after tumor challenge. Percentages of gated cells are shown as mean ± SD in the dot plots in (B), (G), and (H). Data shown in all graphs are representative of three independent experiments, and *P* values were determined with unpaired Student's *t* test [(B) and (E) to (H)] or one-way ANOVA (I). $^{**}P < 0.01$; $^{***}P < 0.001$; $^{****}P < 0.0001$.